Vehicle System Dynamics

International Journal of Vehicle Mechanics and Mobility

ISSN: 0042-3114 (Print) 1744-5159 (Online) Journal homepage: www.tandfonline.com/journals/nvsd20

Longitudinal surge of 10000-ton heavy-haul trains on the Baoshen Railway: effects of locomotive consist and adhesion control

Qun Ma , Wei Wei , Yuan Yao & Jiawen Sun

VEHICLE SYSTEM DYNAMICS
https://doi.org/10.1080/00423114.2026.2711733

Longitudinal surge of 10000-ton heavy-haul trains on the Baoshen Railway: effects of locomotive consist and adhesion control

Qun Ma[a], Wei Wei[b], Yuan Yao [a] and Jiawen Sun[a]

[a]State Key Laboratory of Rail Transit Vehicle, Southwest Jiaotong University, Chengdu, People's Republic of China; [b]College of Locomotive and Rolling Stock Engineering, Dalian Jiaotong University, Dalian, People's Republic of China

ABSTRACT

On China's Baoshen Railway, 10,000-ton heavy-haul trains navigating continuous steep grades and sharp curves are frequently plagued by violent longitudinal surge, repeatedly leading to coupler breakage. Traditional macroscopic models have limitations in revealing the multi-scale coupling mechanism of this phenomenon. To the end, a multi-scale coupled simulation model was established, bridging train longitudinal dynamics, multi-body locomotive dynamics, and real-time adhesion control. The analysis indicates that train surge is intimately linked to the nonlinear dynamic instability of the wheel-rail adhesion interface. The impact of locomotive configuration is highly conditional: under constant per-locomotive tractive effort and high adhesion-utilisation conditions, adding locomotives amplify the longitudinal surge response, increasing the maximum coupler force by 41.2% in a $4+0$ consist compared with a $3+0$ consist. However, distributing the same traction demand across more locomotives reduces the adhesion utilisation of each locomotive and improves the longitudinal dynamic response. Moreover, although adhesion control effectively caps peak transient loads (yielding an 18.4% reduction in maximum coupler force), its frequent torque adjustments introduce repeated low-frequency traction disturbances into the train longitudinal system. This strengthens the coupling between adhesion-control intervention and longitudinal coupler-force fluctuation, exacerbating the surge tendency and driving a severe 58.4% surge in coupler force fluctuation amplitude.

ARTICLE HISTORY
Received 13 April 2026
Revised 9 June 2026
Accepted 13 July 2026

KEYWORDS
Train surge; stick-slip vibration; wheelset drive system; adhesion control; longitudinal dynamics

1. Introduction

As a strategic core corridor for China's 'west-to-east coal transportation', the Baoshen Railway plays an irreplaceable role in the national energy transport system [1]. In recent years, with the rapid advancement of heavy-haul transportation technology, the routine operation of 10,000-ton combined trains has significantly unlocked the railway's capacity potential [2]. However, the Shenmu–Shuozhou section of the Baoshen Railway traverses the complex mountainous terrain of the Loess Plateau, where the combination of 12‰

CONTACT Yuan Yao yyuan8848@163.com

long steep grades and sharp curves challenges the safe handling of extra-long heavy-haul trains [3]. Particularly on uphill sections, high-power locomotives are often arranged in a '3 + 0'(three units, six locomotives) consist configuration. Under the heavy load and the substantial system inertia caused by long train formations, trains are highly susceptible to intense and difficult-to-control longitudinal surge, which greatly affects operational safety [4]. These violent oscillations manifest as sudden large-amplitude fluctuations in longitudinal coupler forces (hereinafter referred to as coupler force) that propagate along the train, accelerating fatigue damage to draft gears and frequently leading to coupler fracture [5–7]. Therefore, revealing the underlying excitation mechanisms of this surge phenomenon and developing effective control strategies are critical scientific imperatives in heavy-haul railway dynamics.

Extensive and systematic research has been conducted in the field of heavy-haul train longitudinal dynamics. At the macroscopic system level, the theoretical foundations were established by Cole [8,9], Garg and Dukkipati [10], and Iwnicki [11]. Building on this foundation, scholars have carried out refined modelling of key components, covering the nonlinear characteristics of friction and polymer draft gears [12–14], the dynamic behaviour of couplers [15], and the coupled simulation of air brake systems with longitudinal dynamics [16]. Among these, the most critical aspect of refined modelling is the air brake system model, which is the primary contributor to simulation accuracy. As reviewed by Wu et al. [17,18], train air brake models can be classified into three categories: empirical models [19–21], fluid dynamics models [22–24], and hybrid fluid–empirical dynamic models [25–27]. System-level simulation platforms developed within this framework, such as TABLDSS [28], have been successfully applied to 20,000-ton heavy-haul trains on China's Daqin and Shuohuang railways, providing crucial support for operational safety. While these macroscopic simulators excel in evaluating braking strategies, they typically simplify locomotives as ideal traction force nodes.

In terms of wheel–rail adhesion characteristics, researchers have investigated in depth the adhesion behaviour and its influence on traction performance based on Kalker's rolling contact theory [29] and Polach's fast algorithm [30–32]. Further studies have extended to the mechanisms of suspension parameters on re-adhesion performance [33,34] and adhesion control strategies under electromechanical coupling [35–37]. However, such studies have mostly focused on adhesion optimisation at the wheelset–track local system level and have yet to be deeply coupled with train longitudinal dynamics.

Regarding specialised research on surge problems, in light of the frequent surge phenomena observed on the Shenshuo Railway, some scholars have begun to investigate the underlying mechanisms and control strategies under specific operating conditions. Various suppression approaches have been proposed, including those based on variations in buffer impedance characteristics [38], signal feature identification [39], and optimisation of longitudinal impulse indices [40]. The potential application of physics-informed machine learning has also been explored. Nevertheless, overall research on surge phenomena in heavy-haul freight trains remains limited, both domestically and internationally. Existing studies are still largely constrained within the framework of macroscopic longitudinal dynamics, and the fundamental causes of surge occurrences, as well as effective mitigation measures, are still not well understood.

Field data indicates that under low-adhesion conditions (e.g. rain or continuous sharp curves), frequent sanding operations cause sharp fluctuations in the wheel-rail friction coefficient [32]. However, existing research models typically simplify the locomotive as an ideal traction force node, critically overlooking these complex wheel-rail interactions – even though surge phenomena predominantly occur under these exact environmental conditions. Therefore, this paper argues that the surge of 10,000-ton trains is closely related to the nonlinear dynamic instability of locomotive wheel–rail adhesion. Under high-power multi-locomotive traction, the adhesion fluctuations induced by frequent sanding not only cause traction force oscillations but also readily trigger stick-slip vibration in the wheelset drive system [33]. During the alternating stick–slip process, the system continuously accumulates torsional elastic potential energy; once this energy exceeds the stability boundary, intense stick-slip oscillations are excited [34], resulting in a sudden increase in locomotive longitudinal acceleration. The alternating impact forces act back on the locomotive, further aggravating secondary wheel–rail slip and load reduction, thereby forming a self-sustaining cycle. As surge energy is continuously injected, transient loads superimpose on the baseline tensile loads, pushing the coupler forces beyond the yield strength and ultimately leading to coupler fracture.

Conventional lumped-mass train models are effective tools for analysing macroscopic train longitudinal dynamics and surge responses. However, when the surge excitation is associated with local wheel–rail adhesion instability, drive-system stick–slip vibration, and transient traction-force fluctuations, representing the locomotive simply as an ideal traction-force input may be insufficient to reveal the underlying formation and transmission mechanism. Therefore, this paper proposes a high-fidelity multi-scale co-simulation framework. By deeply integrating a detailed locomotive multi-body dynamics model (SIMPACK) with a 10,000-ton train longitudinal dynamics model and a real-time adhesion control system (MATLAB/Simulink), this framework enables cross-scale dynamic simulation from local wheel-rail adhesion behaviour to global train longitudinal response.

The remainder of this paper is organised as follows: Section 1 outlines the stick-slip vibration theory. Section 2 analyzes field data of surge-induced coupler fractures on the Shenshuo Railway. Section 3 details the multi-scale co-simulation framework. Section 4 systematically investigates the factors influencing train surge, including traction load, locomotive configuration, and adhesion control strategies. Finally, Section 5 draws the main conclusions.

2. Theory of locomotive stick-slip vibration

The slip ratio, a key parameter of wheel–rail kinematics, is defined in locomotive drive dynamics as [33]:

$$s = \frac{v - \omega r}{v} = 1 - \frac{(\omega_0 + \frac{d\theta}{dt})r}{v_0 + \frac{dx}{dt}} \tag{1}$$

Where v and v_0 represent the instantaneous speed and the mean speed of the wheelset, respectively; ω and ω_0 denote the instantaneous angular velocity and the mean angular velocity, respectively; r is the radius of wheel.

The slip s can be expressed as:

$$s = s_0 + ds \tag{2}$$

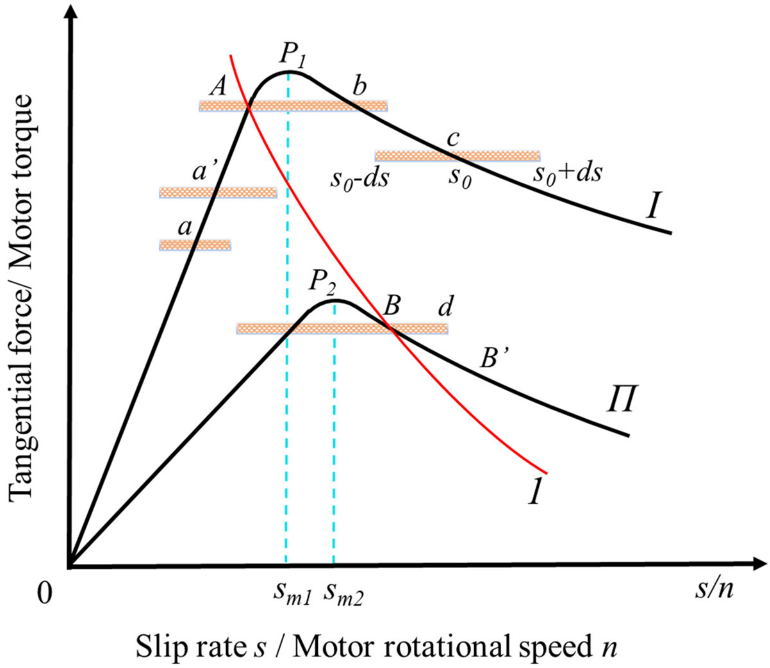

Figure 1. Stick-slip vibration mechanism.

Here, s_0 and ds represent the mean slip and dynamic slip, respectively. s_0 depends on braking/traction and adhesion conditions. The magnitude of ds is considered to be related to the vibration energy, as well as the stiffness and damping characteristics of the elastic connections within the wheelset drive system structure.

Figure 1 illustrates the stick-slip instability mechanism. The solid red line represents the mechanical characteristic curve of the traction motor, while the solid black lines '*I*' and '*II*' denote the wheel–rail creep characteristic curves under dry and wet conditions, respectively. When the locomotive operates at a stable operating point *A* (the intersection of the motor's mechanical characteristic curve and the dry rail creep curve '*I*'), sudden deterioration of rail surface adhesion due to rainfall or negotiation of sharp curves causes the wheel–rail creep curve to shift abruptly from '*I*' to '*II*'. At this point, the motor's mechanical characteristic curve intersects the new creep curve '*II*' at point B. The critical issue lies in the fact that point *B* lies on the negative slope region (slip region) of the creep characteristic curve, which is intrinsically unstable – any minor disturbance will trigger accelerated slipping of the wheelset, leading to a sudden release of the elastic potential energy accumulated within the drive system.

Stick-slip vibration is essentially a nonlinear dynamic transitional state. Its ultimate evolution path – whether it returns to a stable adhesion state or develops into sustained macroscopic sliding – depends entirely on the system parameters and the energy dissipation mechanism. It is particularly noteworthy that during the critical process of wheel–rail adhesion recovery (such as the increase in friction coefficient following sanding), if the structural stiffness and damping of the drive system are insufficiently designed, the system is prone to evolve from a sliding state (state *c*) into a stick-slip vibration state (state *b*).

3. Problem statement and field observations of train surge

The Baode–Wangjiazhai section of the Shenshuo Railway is a highly surge-prone area, characterised by continuous long steep gradients exceeding 11‰, sharp S-curves, and multiple neutral sections. When trains coast through these neutral sections, the main circuit breaker disconnects, causing a sharp reduction in train speed to typically 35–45 km/h. To recover speed and maintain line capacity, locomotives immediately apply high-power traction, inadvertently creating a latent risk of severe longitudinal surge.

Figure 2 presents onboard field records from a 10,000-ton train (driven by a 3 + 0 consist) in which a longitudinal surge event was followed by train separation due to failure of the coupler connection system. The data were obtained from the locomotive's Train Running Monitoring and Recording Device (LKJ, the onboard 'black box'). It should be noted that the LKJ is an event-triggered safety recording system rather than a fixed-sampling-rate data logger; records are generated only when operating states change significantly or safety thresholds are crossed. Consequently, the time intervals between consecutive data points are irregular, and the system does not directly record acceleration signals. The data shown in the figure are raw records without resampling, interpolation, filtering, or other post-processing. Before the critical fracture point at 07:50:53 (indicated by the gray solid line), the locomotive speed (blue line) experienced three noticeable fluctuations, at approximately 07:50:25, 07:50:33, and 07:50:50. Crucially, the amplitudes of these speed fluctuations increased gradually, while the intervals between successive fluctuations became shorter. This temporal evolution suggests that the longitudinal dynamic response of the train was becoming increasingly pronounced before the separation. In addition, the brake pipe pressure did not decrease to zero within the displayed time window because the LKJ record only covers the early stage after train separation. After the separation at approximately 07:50:53, the brake pipe pressure dropped rapidly from approximately 590–560 kPa to about 270 kPa by 07:50:54, while the brake pipe was still venting and had not yet fully exhausted. Therefore, the nonzero pressure shown in Figure 2 is due to the limited displayed time window, rather than a cessation of pressure decrease.

With the arrival of the fourth oscillation peak, the longitudinal dynamic load at the coupler connection increased sharply, leading to train separation. This separation event is instantly corroborated by the system data: the brake pipe pressure (red line) plummeted abruptly from approximately 600 kPa to under 300 kPa due to the rupture of the main air pipe, triggering an emergency brake application. Simultaneously, the locomotive experienced an abnormal, sudden spike in speed due to the instantaneous loss of the massive trailing load. These field measurements confirm the occurrence and development of a severe longitudinal surge event that ultimately led to train separation. It should be noted that Figure 2 mainly provides onboard speed and brake-pipe pressure data; therefore, it directly supports the identification of the longitudinal surge and train-separation process, rather than independently measuring all boundary conditions or identifying the specific failed component of the coupler assembly. The associated high traction demand, low-adhesion risk, and complex track alignment should be understood as the relevant operating and route background of this event, rather than as conditions independently confirmed by the onboard data shown in Figure 2.

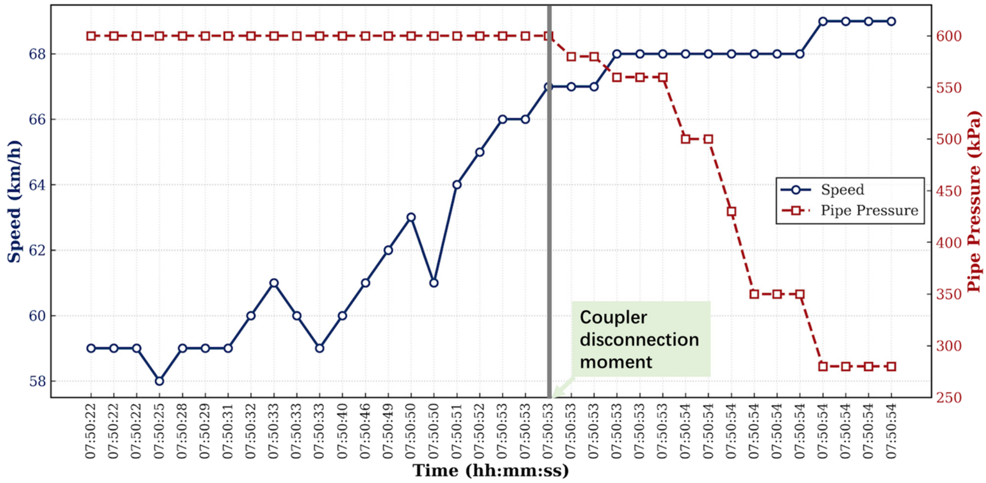

Figure 2. Actual speed and train pipe pressure during surge.

4. Simulation model

Using SIMPACK and MATLAB/Simulink, this study developed a multi-scale framework coupling train longitudinal dynamics, locomotive multi-body dynamics, and adhesion control system (Figure 3). Within the system architecture, MATLAB/Simulink hosts the longitudinal train dynamics model (representing a single-consist 10,000-ton heavy-haul train) and the locomotive adhesion control module, while SIMPACK is utilised to build a high-fidelity locomotive multi-body dynamics model.

A traction calculation module uses locomotive velocity feedback to convert initial commands into motor torque for adhesion control system. This system dynamically adjusts the rotor torque based on real-time monitoring of wheelset kinematics and creep speed. Furthermore, to effectively integrate the locomotive dynamics model with the train longitudinal dynamics model, a coordinated method utilising TCP/IP communication via the Simat interface is employed. By setting a synchronised simulation step, locomotive acceleration data extracted from SIMPACK is transmitted to the Simulink longitudinal dynamics model, while the coupler forces computed by the longitudinal model are returned to the SIMPACK locomotive model in real time.

This bidirectional real-time interaction not only ensures accurate transfer of traction and coupler forces but also establishes a closed-loop dynamic coupling between the locomotive and the train. The approach faithfully simulates the actual power transmission process during locomotive-hauled train operation, effectively capturing the interactive effects among wheel-rail adhesion, coupler forces, and longitudinal dynamics – interdependencies that are difficult to reproduce with traditional single-domain models. The resulting framework providing a high-fidelity platform for traction control research under complex scenarios in heavy-haul railways. The following sections detail the implementation of each module within this multi-scale coupled model.

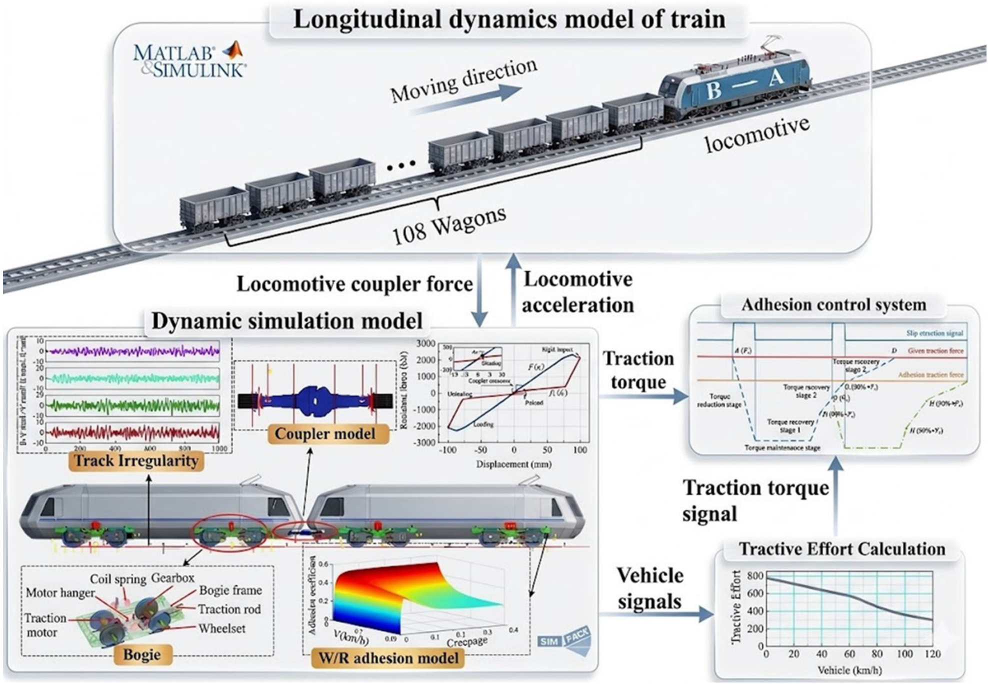

Figure 3. Multiscale train-locomotive-adhesion coupling framework.

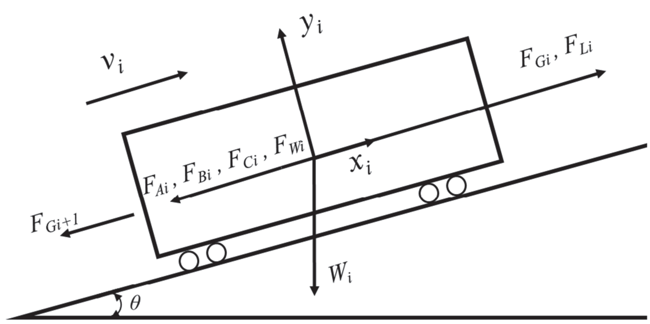

Figure 4. The force diagram of single vehicle.

4.1. Longitudinal dynamic model

4.1.1. Vehicle force analysis

In the simulation system, each locomotive (or vehicle) is regarded as a concentrated mass, and each vehicle is connected by a spring-damping unit. The force analysis of any vehicle i is shown in Figure 4.

Each vehicle has the following force equilibrium equation:

$$F_i^{pre} = F_{Gi} - F_{Gi+1} + F_{Li} - F_{wi} \tag{3}$$

$$m_i a_i = F_i^{pre} + F_i^{res,eq} \tag{4}$$

$$F_i^{res,eq} = \begin{cases} -\dfrac{v_i}{|v_i|}(F_{Ai} + F_{Bi} + F_{Ci}) & v_i > 0 \\ -(F_{Ai} + F_{Bi} + F_{Ci}) & v_i = 0 \quad and \quad F_i^{pre} \geq (F_{Ai} + F_{Bi} + F_{Ci}) \\ -F_i^{pre} & v_i = 0 \quad and \quad F_i^{pre} < (F_{Ai} + F_{Bi} + F_{Ci}) \\ 0 & v_i = 0 \quad and \quad F_i^{pre} = 0 \end{cases} \tag{5}$$

Where $F_i{}^{pre}$ denotes the preliminary longitudinal resultant force acting on vehicle (i) before applying the running-resistance balance. It mainly includes the difference between the front and rear coupler forces, the traction/electric braking force, and the grade resistance. $F_i{}^{res,eq}$ denotes the equivalent resistance term, which describes the effect of the basic running resistance, air braking force, and curve resistance on the longitudinal motion of vehicle (i) under moving or stationary conditions. $m_i\ddot{x}_i$ denotes the inertial force of vehicle i; F_{Li} denotes the traction (or electric braking) force; F_{Gi} and F_{Gi+1} denote the coupler forces acting on the two ends of vehicle i; F_{Bi} denotes the air braking force; F_{Ci} denotes the curve resistance; F_{Ai} denotes the basic running resistance; and F_{Wi} denotes the grade resistance. By solving the equations of equation (4) at any time, the physical state and forced condition of each locomotive and vehicle of the train can be obtained. According to Chinese railway standard [41], Train Traction Calculation (TB/T 1407.1-2018), the basic operating resistance is as follows (6)-(7):

$$F_{A\_W} = 0.92 + 0.0048v + 0.000125v^2 \tag{6}$$

$$F_{A\_Loc} = 1.40 + 0.0038v + 0.00013v^2 \tag{7}$$

Where $F_{A_w}$is the basic running resistance of C80 freight wagon (N/kN) and F_{A_Loc} is the basic running resistance of the locomotive (N/kN). However, it was found during calculation that the resistance coefficients in 'Train Traction Calculation (TB/T 1407.1-2018)' are not entirely applicable. Therefore, without changing the form of Eq. (6), the basic running resistance F_A formula was re-determined based on test data using the ant colony algorithm [42], as shown in Eq. (8). The derivation process, algorithm details, and related verification of this formula can be found in Reference [42].

$$F_A = 0.785 + 4.153 \times 10^{-3}v + 1.551 \times 10^{-6}v^2 \tag{8}$$

4.1.2. Freight wagon draft gear model

The MT-2 friction-type draft gear model adopted in this paper originates from a piecewise linear friction-type draft gear dynamic model established and validated in Refs. [43,44]. That model was developed based on MT-2 draft gear vehicle impact test data, combined with the loading, unloading, and transition process characteristics of friction-type draft gears. The model parameters were identified and validated against the corresponding impact test data. To ensure the completeness and clarity of the draft gear force calculation process in the longitudinal dynamics model of this paper, the main formulation of the model is briefly described below.

(1) Loading process resistance force

When $\Delta x \cdot (d\Delta x/dt) > 0$, the draft gear is in the loading process. During the loading process, the resistance force curve of the draft gear exhibits typical piecewise characteristics, which are described in the model using multiple linear segments. Specifically, the loading curve within the draft gear stroke is discretized into n segments, each described by a linear function. A larger value of n allows the model to more closely approximate the impact test curve. The resistance force F_u of the draft gear during loading is expressed as:

$$\begin{aligned} &F_u = F_0 + \sum_{j=1}^{i-1} k_j(s_{j+1} - s_j) + k_i(\Delta x - s_i) \\ &\Delta x * \frac{d\Delta x}{dt} > 0 \; and \; \frac{dx}{dt} > v_e \; and \; s_i < \Delta x \leq s_{i+1} \end{aligned} \tag{9}$$

Where Δx is the actual compression of the draft gear; s_i are the abscissas of the segment points on the loading curve; $k_1, \ldots, k_i$ are the slopes of the respective segments; and F_0 is the initial pressure of the draft gear. where v_e is the critical velocity, serving as the threshold for controlling the transition of the draft gear between static and dynamic states.

Due to the presence of initial pressure in the draft gear, the resistance force at the beginning of the loading curve exhibits a jump, which often leads to oscillations in the coupler force during simulation and even render the calculation unstable. To address this issue, the model replaces the initial pressure with a specific function curve. Within a small range of compression, the resistance force gradually increases along this curve to the initial pressure, thereby ensuring the continuity of the loading curve. Considering that the exponential function is characterised by a nonlinear variation with the independent variable, the specific function is constructed as an exponential function of the compression amount when the coupler slack is not taken into account. The exponential function is defined as Eq. (10):

$$\begin{aligned} &F_0 = \omega(1 - e^{|-\tau\Delta x|}) \\ &\Delta x * \frac{d\Delta x}{dt} > 0 \; and \; 0 < \Delta x < x_0 \; and \; \frac{d\Delta x}{dt} > v_e \end{aligned} \tag{10}$$

Where ω is the coefficient controlling the magnitude of the initial pressure; τ is the coefficient controlling the rate of change of the resistance force; x_0 is the valid range of the function.

At the end of the loading curve of the friction-type draft gear, the resistance force exhibits a sharp increase known as the peak effect. This phenomenon is caused by velocity-dependent friction. When the compression speed of the draft gear is very low, the internal friction mechanism enters a transition state from dynamic friction to static friction, causing the resistance force to increase rapidly and the stiffness of the characteristic curve to become progressively larger. After the loading process ends, the friction mechanism of the draft gear remains in a static locked state. To simulate this peak effect, the adopted model uses a velocity-dependent exponential compensation function. When the compression speed of the draft gear falls within a certain low range, the compensation function is used to generate an additional resistance force F_e, and the smaller the compression speed, the larger the additional resistance force should be. At this point, the total resistance force of the draft gear is the sum of the resistance force on the loading curve and the additional resistance force. The exponential compensation function is adopted because this type of function can effectively simulate the velocity-dependent friction effect characteristic of dry-friction draft gears. The compensation function is given by Eq. (11).

$$\begin{aligned} F_e &= \frac{\lambda e^{-|\Delta x/v_e|}}{1+e^{-|\Delta x/v_e|}} \\ \Delta x * \frac{d\Delta x}{dt} &> 0 \; and \; \frac{d\Delta x}{dt} < v_e \end{aligned} \tag{11}$$

Where λ is the compensation coefficient, used to control the magnitude of the resistance force; Δx is the compression of the draft gear. where v_e is the critical velocity, serving as the threshold for controlling the transition of the draft gear between static and dynamic states. It should be noted that the transition and compensation parameters in Eqs. (9)–(11), such as v_e, ω, τ, and λ, were not re-identified in this paper, but were directly adopted from the parameters previously identified and validated using MT-2 draft gear impact test data in Refs. [43,44].

(2) Unloading process resistance force

When $\Delta x \cdot (d\Delta x/dt) < 0$, the draft gear begins to enter the unloading process.

$$F_d = k_{dw}\Delta x \quad \Delta x * \frac{d\Delta x}{dt} < 0 \tag{12}$$

where F_d is the unloading resistance force; k_{dw} is the unloading stiffness; Δx is the compression of the draft gear; and $\Delta \dot{x}$ is the compression velocity of the draft gear.

(3) Transition Process Resistance Force

After loading ends, when $\Delta x \cdot (d\Delta x/dt) < 0$, the draft gear begins to enter the unloading process. During unloading, the direction of the friction force changes, resulting in different characteristics between the loading and unloading curves. However, at the very beginning of unloading, a notable discontinuity appears between the loading and unloading curves, causing an abrupt jump in the draft gear resistance force. The reason is that when unloading starts, the friction mechanism is still in a static locked state, and the relative speed between adjacent vehicles is low. As a result, the friction mechanism cannot unlock and move immediately, leading to a significant displacement lag. The unloading curve drops directly along the vertical axis of displacement x, causing the draft gear to release all its force instantaneously. This results in a jump in the resistance force, which even fall below the coupler forces observed in other stages of unloading. This phenomenon is referred to as 'locked unloading'. To address the 'locked unloading' phenomenon caused by displacement hysteresis during the loading-to-unloading transition, the model employs a method of displacement compensation together with an additional hysteresis resistance force, so that the characteristic curve of the transition phase gradually returns to the unloading curve along a specific path. The advantage of this approach is that during repeated loading and unloading cycles of the draft gear, a distinct hysteresis loop appears on the characteristic curve of the transition phase, reflecting the energy dissipation behaviour of the draft gear. The transition resistance force F_g is calculated using Eqs. (13) and (14).

$$F_g = F_m + k'(\Delta x_t - \Delta x_m) + F'_g \qquad \Delta x* \left(\frac{d\Delta x}{dt}\right) < 0 \; and \; F_g > F_d \tag{13}$$

$$F'_g = \mu_c(\Delta x_t - \Delta x_{t-\Delta t}) \tag{14}$$

where $F_g{}'$ is the additional hysteresis resistance force generated during displacement compensation; μ_c is the compensation coefficient; Δx_t is the compression of the draft gear at the current time; k' is a constant representing the stiffness during this transition phase; F_m is the maximum coupler force during the current loading cycle; Δx_m is the compression corresponding to the maximum coupler force during loading; F_d is the unloading resistance force, which is calculated using Equation (12). The parameters k' and μ_c are used to control the transition stiffness and displacement compensation characteristics during the loading–unloading transition process, and their values are also adopted from the validated parameter set in the studies [44]. Figure 5(A) shows the impedance characteristics of a single draft gear at the contact interface between the impacting car and the impacted car under the condition of 8 km/h impact speed and four impacting cars, obtained from the model with transition phase treatment. It can be observed that at the beginning of unloading, a distinct hysteresis loop appears on the draft gear impedance characteristic curve, dissipating part of the impact energy. A more detailed description can be found in Reference [43].

Therefore, the formula for calculating the draft gear resistance force is as follows:

$$F = \begin{cases} F_u & \Delta x * \dfrac{d\Delta x}{dt} > 0 \; and \; \dfrac{d\Delta x}{dt} \geq v_e \\ F_u + F_e & \Delta x * \dfrac{d\Delta x}{dt} > 0 \; and \; \dfrac{d\Delta x}{dt} < v_e \\ F_g & \Delta x * \dfrac{d\Delta x}{dt} < 0 \; and \; F_g > F_d \\ F_d & \Delta x * \dfrac{d\Delta x}{dt} < 0 \; and \; F_g \leq F_d \end{cases} \tag{15}$$

The switching logic in Eq. (15) can be explained as follows. The model first determines whether the draft gear is in a loading or unloading tendency based on the sign of $\Delta x \cdot (d\Delta x/dt)$. When $\Delta x \cdot (d\Delta x/dt) > 0$, the draft gear is in the loading process, and the loading resistance force F_u is adopted. In this process, the velocity threshold v_e is used to judge whether the velocity-dependent effect is significant and to control whether the peak compensation term is activated, thereby simulating the resistance force peak effect that occurs at the end of loading in a friction-type draft gear. When $\Delta x \cdot (d\Delta x/dt) < 0$, the draft gear begins to enter the unloading process. Due to the reversal of the friction direction and the displacement hysteresis, the resistance force cannot jump immediately from the loading curve to the unloading curve. Therefore, when $F_g > F_d$, the transition resistance force F_g

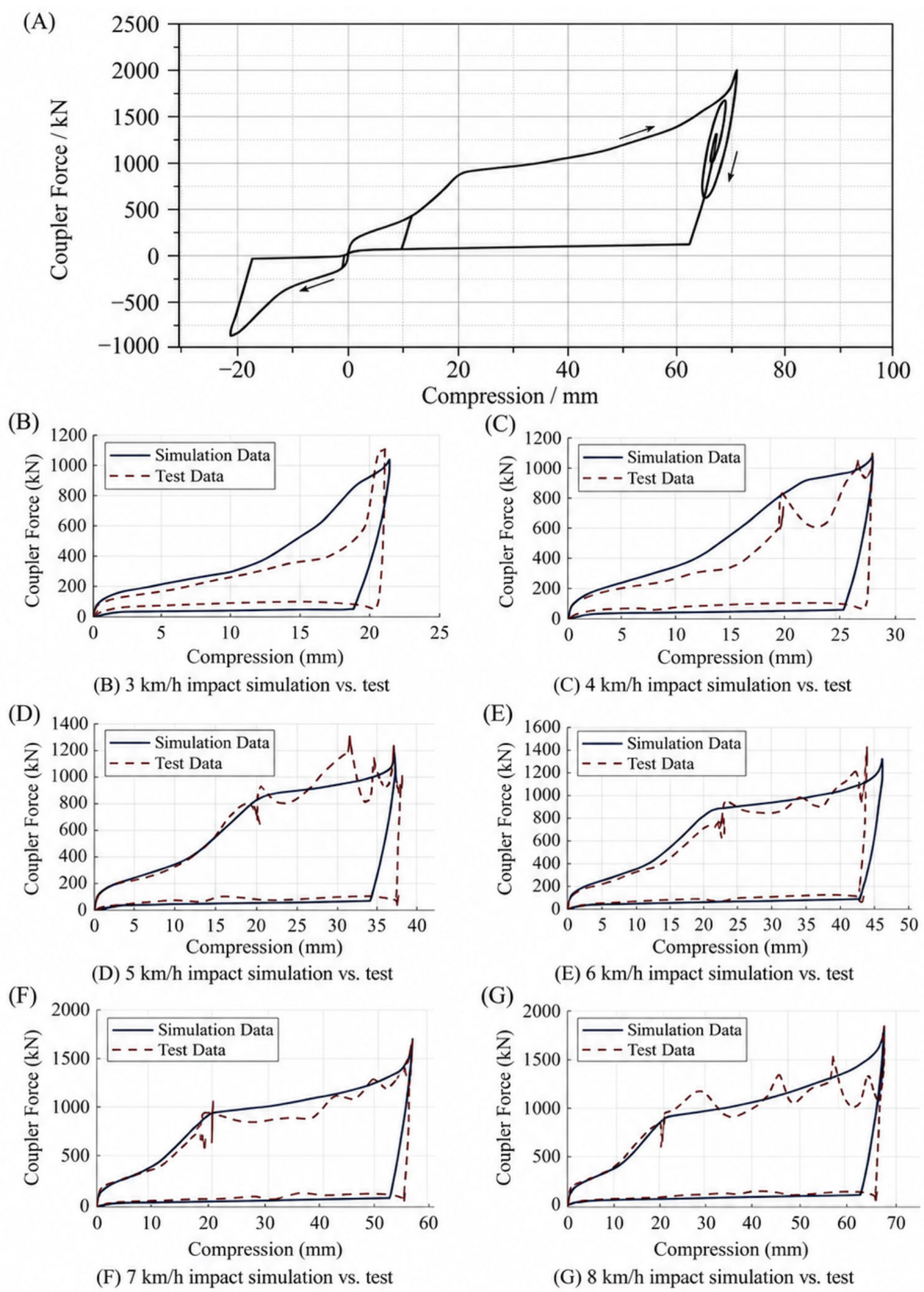

Figure 5. Characteristic curve of draft gear under impact test.

is used, indicating that the current transition curve still lies above the unloading curve and the model remains in the loading–unloading transition stage. When $F_g \leq F_d$, the transition curve has returned to or fallen below the unloading branch, and the model exits the transition stage and switches to the unloading resistance force F_d. This treatment ensures the continuity of the resistance force during the loading–unloading transition and avoids abrupt force changes or the locked unloading problem.

The conversion between coupler force and draft gear resistance force is shown in Equation (15).

$$F_c = \begin{cases} |F| & x \geq 0 \\ -|F| & x < 0 \end{cases} \tag{16}$$

where F_c is the coupler force; F is the draft gear resistance force; and x is the relative displacement between two adjacent vehicles.

As can be seen from Figure 5, the model effectively simulates the characteristics of the draft gear, including preload, loading, peak effect, and unloading. Moreover, during the transition from loading to unloading, the coupler force decreases along a certain transition curve, ensuring the continuity of the draft gear impedance characteristics. A comparison between the simulation results and the test results shows that the variation trends of the two are generally consistent, with only some differences in local data points and compression amounts, such as in the second half of the loading process. The main reason is that the friction surfaces of the internal friction mechanism of the draft gear exhibit significant hysteresis damping, leading to irregular variations in the impedance force.

4.2. Locomotive model

Based on actual locomotive parameters, a multi-body dynamics model of a double-unit heavy-haul locomotive was developed using SIMPACK. The locomotive employs an axle-hung drive system (also known as a nose-suspended motor), comprising wheelsets, axle boxes, traction motors, gearboxes, and motor suspension components. The configuration consists of two locomotives connected by a Type 100 arc-shaped coupler [45] equipped with an elastomeric gel draft gear, the specific parameters of which are provided in Section 3.2.2. Key suspension parameters of the locomotive are summarised in Table 1.

4.2.1. Wheel-rail adhesion characteristics

The adhesion condition at the wheel-rail interface has minimal impact on the normal contact but significantly influences the frictional characteristics and tangential interaction. A widely adopted friction model in locomotive drive dynamics was proposed by Polach [30]. The corresponding formulation is as follows:

$$\mu = \mu_0[(1 - A)e^{-Bs_{wr}} + A] \tag{17}$$

In the equation, μ represents the rail surface friction coefficient, μ_0 denotes the maximum friction coefficient at zero sliding velocity, s_{wr} is the total relative sliding velocity between the wheel and rail, A is the ratio of the friction coefficient μ_∞ at infinite sliding velocity to μ_0, and B is the friction decay coefficient.

By changing the friction parameters μ_0, A, and B, together with the Kalker reduction factors denoted by k_A and k_s, different adhesion curves can be simulated. The coefficients k_A and k_s are the reduction factors of the Kalker coefficients in the adhesion and sliding regions, respectively. They satisfy ($0 < k_A \leq k_s \leq 1$), and are used to describe the nonlinear reduction of the tangential creep force relative to that predicted by Kalker's linear theory under practical wheel-rail contact conditions.

Table 1. Main parameters of the locomotive's dynamic model.

Physics mean	Value
Axle load (t)	25
Bogie wheelbase (m)	2.9
Distance between bogie centers (m)	9
Mass of the car body (kg)	61880
Roll inertia of the car body (kg m^2)	95970
Pitch inertia of the car body (kg m^2)	1539900
Yaw inertia of the car body (kg m^2)	1536740
Mass of the bogie frame (kg)	6000
Roll inertia of the bogie frame (kg m^2)	2886
Pitch inertia of the bogie frame (kg m^2)	10672
Yaw inertia of the bogie frame (kg m^2)	13031
Wheelset mass (kg)	1353
Pitch inertia of the wheelset (kg m^2)	458
Mass of the motor stator (not including rotor of motor) (kg)	2910
Pitch inertia of motor stator (not including rotor of motor) (kg m2)	318
Mass of the rotor (kg)	650
Pitch inertia of the rotor (kg m2)	18
Small gear mass (kg)	120
Pitch inertia of the small gear (kg m2)	2.3
Big gear mass (kg)	360
Pitch inertia of the big gear (kg m2)	24
Longitudinal distance from stator mass center to wheelset(m)	0.543
Longitudinal distance from the motor suspension rod to wheelset(m)	1.045
Primary longitudinal stiffness(kN/mm)	36
Gearbox suspension stiffness(kN/mm)	50
Torsional stiffness of gear coupling (MNm/rad)	13.5
Transmission ratio of gear transmission	6.24

The wheel-rail tangential force can be expressed as follows:

$$F_a = \frac{2\mu Q}{\pi}\left[\frac{k_A\varepsilon}{1+(k_A\varepsilon)^2} + \arctan(k_s\varepsilon)\right] \tag{18}$$

Where Q is the wheel weight. F_a is the wheel-rail tangential creep force, μ is the wheel-rail friction coefficient. The parameter ϵ represents the nonlinear argument associated with the tangential stress gradient in the adhesion region and is evaluated according to Polach's formulation. In this study, k_A, k_s, and the relevant friction parameters were adopted from Ref. [30].

4.2.2. Elastomeric gel buffer model

According to Ref. [46], the hysteresis characteristics of the coupler buffer can be represented by the loading and unloading force-displacement curves $f_l\ (x_c)$ and $f_u(x_c)$. The impedance force of the coupler buffer can be expressed as [46]:

$$F_c(x_c, \Delta v) = \begin{cases} \frac{1}{2}[f_u(x_c) + f_l(x_c)] + \frac{1}{2}[f_u(x_c) - f_l(x_c)]\mathrm{sign}(\Delta v)\ |\Delta v| \geq ev \\ \frac{1}{2}[f_u(x_c) + f_l(x_c)] + \frac{1}{2}\frac{\Delta v}{ev}[f_u(x_c) - f_l(x_c)]\mathrm{sign}(\Delta v)\ |\Delta v| < ev \end{cases} \tag{19}$$

Where F_c is the impedance force of the coupler buffer; x_c is the buffer stroke; $f_l\ (x_c)$ and $f_u(x_c)$ are the loading and unloading force–displacement curves, respectively, which are

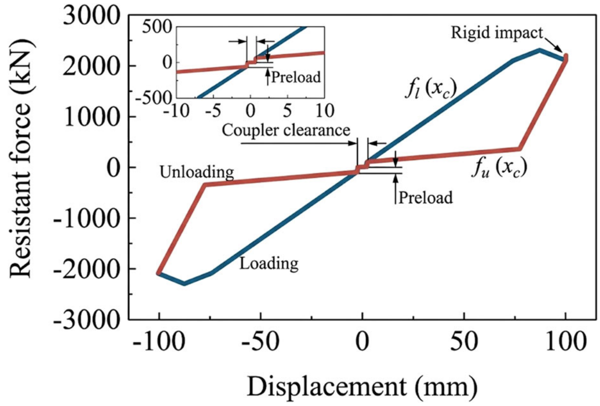

Figure 6. Force-displacement characteristic curve of the coupler buffer.

determined in this study from the impact test and static compression test data of the elastomeric gel buffer; $\Delta v = \dot{x}_c$ denotes the relative velocity between the two connection points of the buffer, and its sign is determined by the variation direction of x_c; ev is the switching velocity threshold in the hysteretic switching model, used to control the continuous transition between the loading and unloading curves; the $sign(\Delta v)$ function is used to select the loading or unloading hysteresis branch according to the direction of relative motion. When $|\Delta v| \geq ev$, the buffer impedance force is output according to the loading or unloading characteristic curve; when $|\Delta v| < ev$ the impedance force transitions continuously with the relative velocity to avoid a sudden force jump during the loading–unloading switch. The nonlinear hysteretic characteristics of the coupler buffer are shown in Figure 6.

4.3. Adhesion control module

At present, the combined correction method is widely used in locomotives in China. Figure 7 shows the adhesion control block diagram of a heavy-haul electric locomotive. It primarily detects wheel pair acceleration/deceleration and creep speed to identify wheel slip/slide conditions and performs control accordingly. The wheel slip/slide criteria and dynamic torque adjustment functions of the adhesion control system are mainly achieved through acceleration protection and creep speed protection strategies. When minor slip occurs, the creep speed protection strategy is employed, using the current wheel pair creep speed as feedback and targeting a preset creep speed to achieve minimum-overshoot control, enabling rapid adhesion recovery during wheel slip/slide. In cases of severe slip, the acceleration protection strategy is adopted to significantly reduce the traction motor torque setpoint, thereby eliminating slip/slide phenomena.

The adhesion protection torque control is divided into three phases: reduction, hold, and recovery. During the recovery phase, a three-stage strategy – fast first, then slow – is employed. In the first stage, torque is restored to 80% of the pre-reduction traction force at a slope of s_1. In the second stage, it recovers to 95% at a slope of s_2. The third stage restores it to 100% of the original traction force at a slope of s_3, with the slopes satisfying the relationship $s_1 > s_2 > s_3$. Between the reduction phase and the recovery phase is the torque maintenance stage, during which the traction force remains constant. If slip is

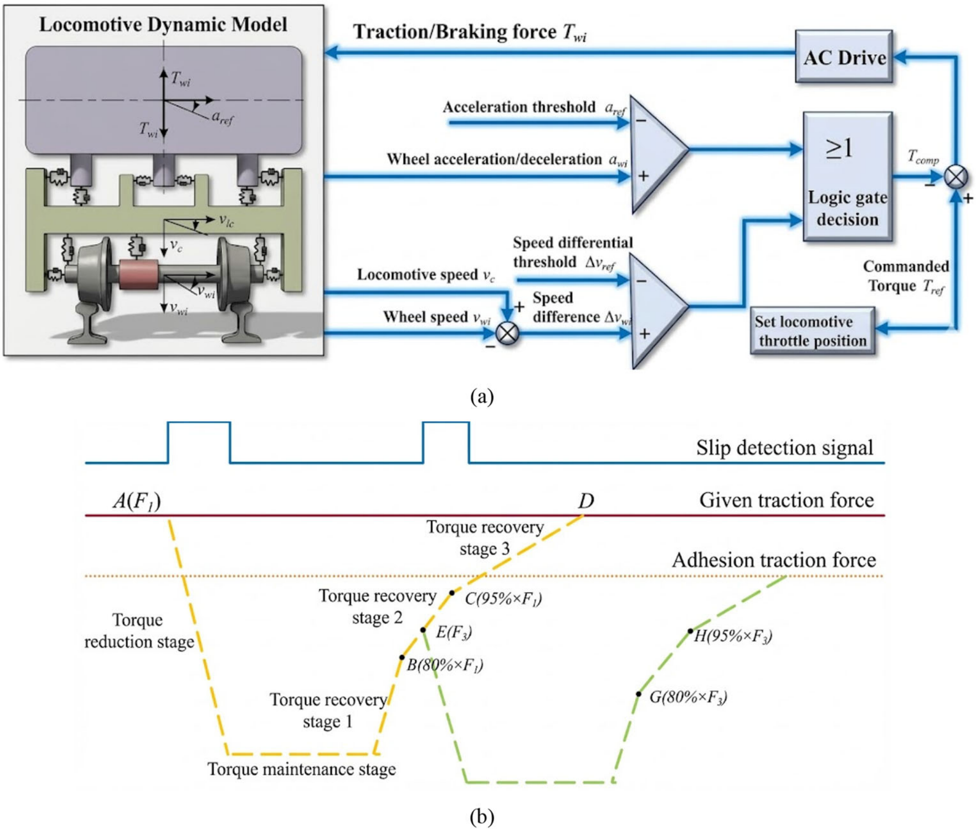

Figure 7. Adhesion control module: (a) Control logic; (b) Torque control logic.

detected during either the hold or recovery phase, the system enters a secondary reduction phase. Through multiple cycles of reduction and recovery, the traction force can gradually approach the currently available adhesion limit.

5. Analysis of factors influencing surge

To systematically investigate the longitudinal surge characteristics, the simulations in this section share a baseline configuration unless otherwise specified: a 10,000-ton train (108 C80 wagons, MT-2 draft gears with 10 mm slack) entering a rainfall-induced low-adhesion section at an initial speed of 60 km/h (as field data indicates that train surge predominantly occurs under such kinematic conditions). Dynamic sanding is simulated by adjusting the rail friction coefficient. To exclude high-frequency external interference, neither rail irregularity excitation nor adhesion is introduced in this simulation.

5.1. Train surge simulation

In this baseline scenario, the train is powered by a '3 + 0' (six locomotives, three units) consist. The target traction output per locomotive is set to 250 kN, yielding a total train traction force of 1500 kN. It significantly exceeds the empirically derived surge-triggering threshold of 1350 kN, yet remains below the ultimate physical traction limit of the leading locomotives (1650 kN). This ensures the simulated operating conditions firmly fall within the highly surge-prone regime while maintaining strict physical rationality.

Figure 8 presents the time-domain evolution characteristics of the longitudinal coupler force (hereinafter referred to as coupler force)at the rear of the first wagon adjacent to the locomotive group during continuous sanding, the locomotive wheelset longitudinal creepage, rail friction coefficient, and wheelset longitudinal vibration acceleration. In the present simulation, the sanding process is represented equivalently by step changes in the wheel–rail friction coefficient. The labels S_1-S_6 in Figure 8 correspond to successive adhesion recovery steps, rather than a detailed physical simulation of actual sand particle motion. The coupler force at this location, rather than at the front end of the first wagon, is selected because it represents the first standard 'wagon–wagon' connection in the train. Compared with the locomotive–wagon interface, which is strongly influenced by the locomotive end, the rear end of the first wagon can more faithfully reflect the nonlinear dynamic response characteristics of a uniform freight car consist. Moreover, this first-wagon location also serves as the starting point for observing how the transient excitation from the locomotive is transformed into longitudinal stress waves and propagated rearward. The wheelset longitudinal vibration acceleration signal shown in Figure 8 is the unfiltered raw output of the coupled SIMPACK–MATLAB/Simulink simulation. The high-frequency vibration around 50 s is a physical stick–slip response induced by wheel–rail adhesion instability and the slip–re-adhesion process rather than numerical noise. Therefore, no filtering was applied in this study, in order to preserve the local vibration characteristics associated with the surge-triggering process.

The simulation results indicate that within the low-adhesion section, as sanding induces a stepwise recovery of the wheel–rail adhesion state, the actual traction force of the locomotive exhibits transient reductions and recoveries. This transient disturbance at the locomotive end directly is reflected in the longitudinal coupler-force response at the adjacent wagon connection and is transmitted through the coupler and draft gear system into the following wagon consist suggesting the initial development of longitudinal surge response near the train head.

A deeper analysis of the nonlinear dynamic evolution of the system reveals that in the early stages of sanding (e.g. $S_1$and S_2), fluctuations in the rail friction coefficient do not yet excite obvious strongly stick–slip vibration. At this stage, the coupler force amplitude is limited, and both the wheelset longitudinal creepage and vibration acceleration remain at low-amplitude convergent levels. However, as continuous sanding progresses, each rapid transition from 'low adhesion to high adhesion' introduces a transient disturbance into the wheelset–drive system, causing dynamic responses of the elastic transmission components and increasing local vibration energy.

During the interval between (S_3) and (S_4), at approximately 45–50s, the wheelset drive system shows a tendency to develop into high-frequency stick-slip oscillation. On the characteristic curves, this stage is manifested as a marked increase in wheelset creepage and longitudinal vibration acceleration, with the wheel–rail interface undergoing high-frequency alternation between adhesion and slip. This high-frequency excitation is transmitted to the adjacent freight-wagon coupler through the coupler and draft gear system. The coupler force sharply drops from 1954.9 kN to 747.1 kN within a very short time,

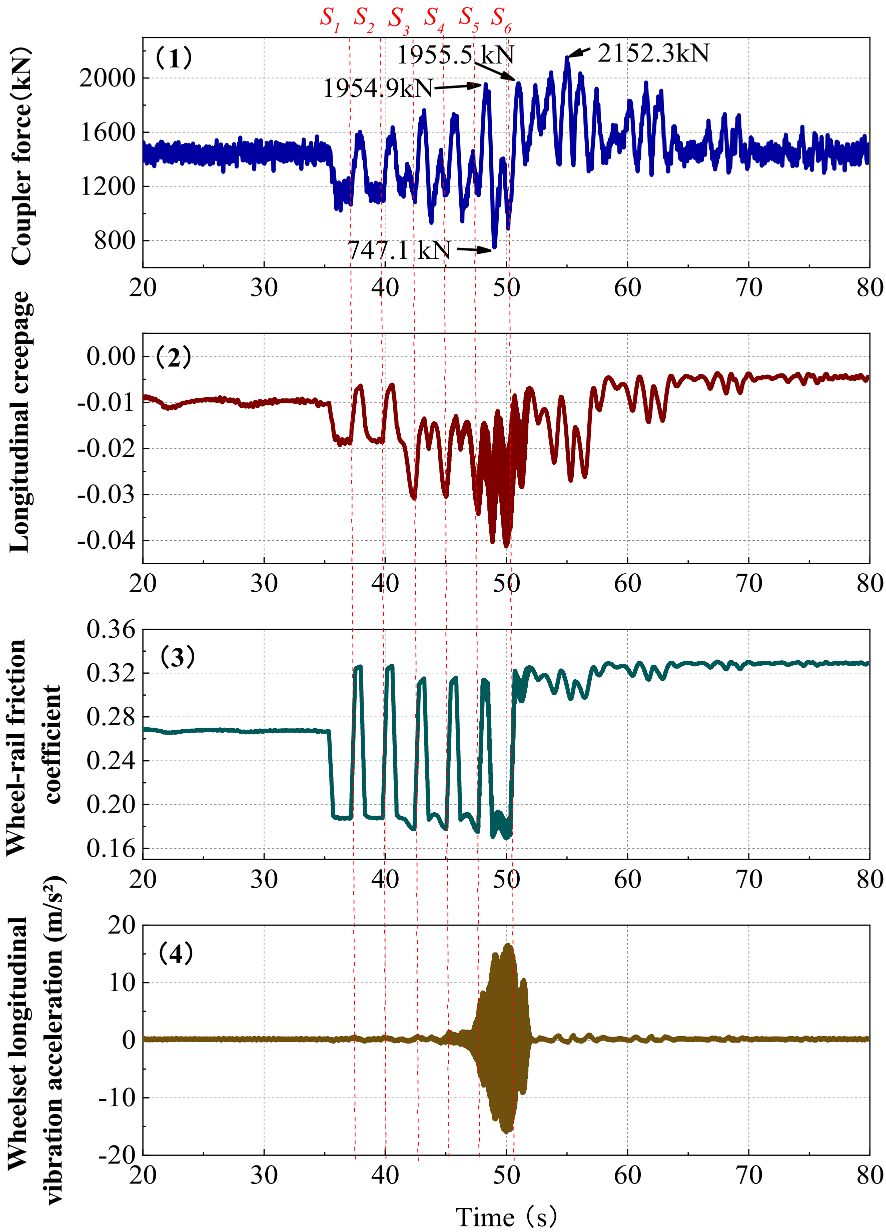

Figure 8. (1) Coupler force at the rear of the first wagon; (2) Wheelset longitudinal creepage; (3) Wheel-rail friction coefficient; (4) Wheelset longitudinal vibration acceleration.

followed by a violent rebound to 1955.5 kN. This abrupt longitudinal load variation indicates that the local stick–slip excitation generated at the locomotive end has significantly affected the front-end longitudinal force response of the train.

Once the wheel–rail adhesion has fully recovered, the drive system re-establishes a dynamic equilibrium; the stick–slip oscillation subsides and the local high-frequency energy dissipates rapidly (after 50s), the stick-slip oscillation subsides, and the local high-frequency energy dissipates rapidly. However, have already injected a transient disturbance into the longitudinal train system, which contribute to the subsequent development of longitudinal surge response. Given the significant system inertia and low inter-car damping of the 10,000-ton train, this low-frequency surge wave persist for a relatively long period in the coupled train longitudinal system. During this evolution cycle, the longitudinal coupler force response at the measuring point shown in Figure 8 is significantly enhanced, indicating that the wheel–rail stick–slip excitation intensify the front-end longitudinal dynamic response of the train after being transmitted through the coupler and draft gear system. The peak dynamic coupler force during the surge phase reaches 2152.3 kN, representing a dynamic overshoot of 43.5% compared to the baseline constant traction condition (1500 kN). This extreme dynamic overload not only accelerates fatigue damage to critical coupler components but also poses a serious threat to train operational safety.

5.2. Effect of total tractive effort

To investigate the influence of total tractive effort on the triggering and amplification of longitudinal surge, this section focuses on the $3 + 0$ locomotive configuration. Here, total tractive effort refers to the total tractive effort output of the locomotive group. Three total tractive effort levels are considered: 1200, 1500, and 1650 kN, corresponding to low-load, medium-load, and full-load conditions, respectively.

Figure 9 illustrates the time-domain evolution trajectories of locomotive coupler force, longitudinal creepage, and longitudinal accelerations of the car body and wheelset. The wheel–rail adhesion coefficient setting used in Figure 9 is the same as that defined in Figure 8. Unless otherwise specified, the following simulations in this section adopt the same prescribed low-adhesion and sanding-induced adhesion-recovery profile. Figure 10 illustrates the locomotive wheel–rail adhesion characteristic curve under different total tractive effort levels. It can be observed that the total tractive effort level has an important influence on the dynamic response of the wheelset–drive system and the longitudinal coupler force.

Under the low-load condition with a total tractive effort set to 1200 kN (red curve), the system response remains relatively stable and shows a sufficient stability margin. The wheel–rail operating point remains within the linear micro-slip region of the adhesion characteristic curve due to the low individual locomotive load. Even when subjected to friction coefficient steps induced by continuous sanding, the wheelset creepage and acceleration remain at very low levels, demonstrating good robustness against the prescribed adhesion disturbances.

Under the medium-load condition, the response shows transient amplification followed by gradual recovery. When the total tractive effort is increased to 1500 kN (blue curve), during the low-adhesion excitation period from 35 s to 50 s, the system exhibits significant transient fluctuations (such as high-frequency oscillations in creepage and local acceleration). However, after the rail surface conditions recover at 50 s, the locomotive drive system gradually returns toward a lower-amplitude response state, and the tractive effort output and coupler force gradually return to a steady state. Nevertheless, during the subsequent recovery process, relatively large longitudinal coupler force peaks and fluctuations are generated, posing a considerable threat to train operational safety.

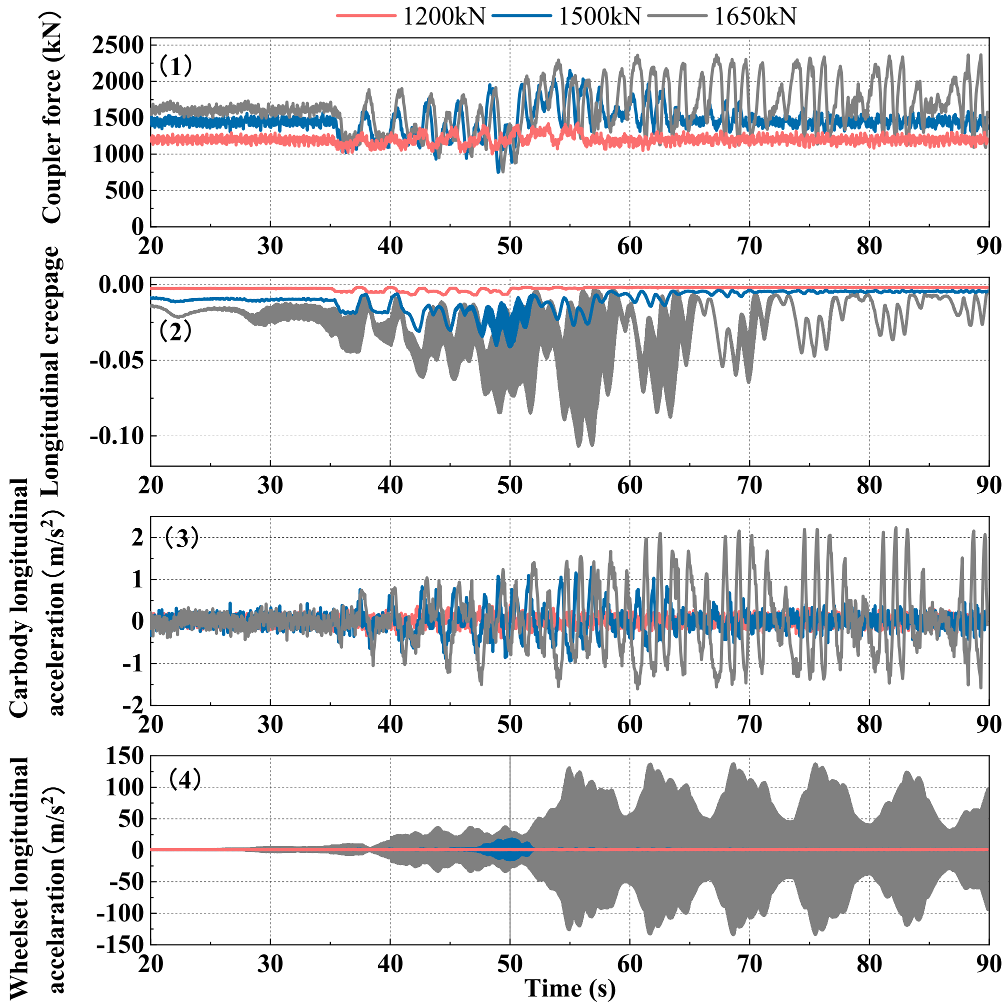

Figure 9. (1) Coupler force at the rear of the first wagon; (2) Wheelset longitudinal creepage; (3) Car body longitudinal vibration acceleration; (4) Wheelset longitudinal vibration acceleration.

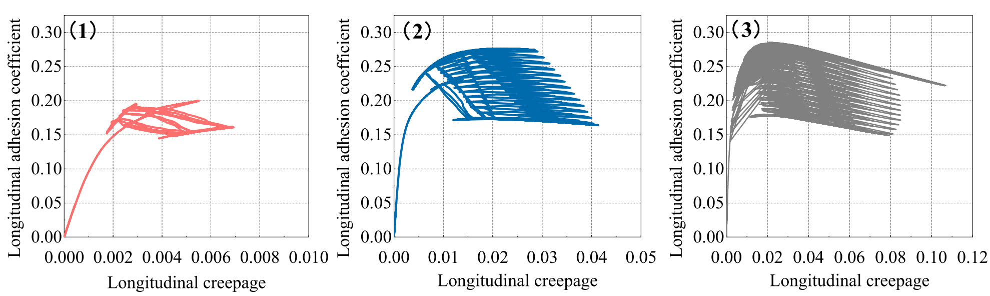

Figure 10. Locomotive wheel–rail adhesion characteristic curves: (1) low load; (2) medium-load; (3) full-load.

Under full-load condition, the system response amplitude increases markedly, and the longitudinal surge becomes more severe. When the leading locomotives operate at a total tractive effort of 1650 kN (gray curve), the dynamic response of the system exhibits a significant increase in oscillation amplitude. The higher tractive effort moves the wheel–rail operating point closer to the unstable region of the adhesion characteristic curve. At this point, adhesion disturbances caused by sanding-induced friction-coefficient steps are more easily amplified, leading to a pronounced increase in wheelset longitudinal creepage.

The wheel-rail adhesion interface shows a tendency toward stick–slip vibration, and the drive system enters a high-frequency stick–slip vibration state, with the peak longitudinal vibration acceleration of the wheelset reaching approximately $\pm 125\,\mathrm{m/s^2}$. This high-frequency excitation also affects the longitudinal vibration response of the locomotive carbody and is transmitted through the coupler and draft gear system to the adjacent freight-wagon connection. As a result, the longitudinal coupler force exhibits large-amplitude fluctuations within a wide range of approximately1000 kN to 2500 kN. After 50 s, although the prescribed sanding-induced adhesion recovery has ended and the wheel–rail adhesion coefficient has become relatively stable, the system under the 1650 kN full-load condition does not return to a low-amplitude response state within the simulated time window.

5.3. *Effect of the number of locomotives*

In the practical operation of 10,000-ton heavy-haul trains on China's Wari and Baoshen Railways, longitudinal surge is rarely observed when trains are hauled by a 2 + 0 consist. Conversely, surge phenomena occur frequently in '3 + 0' consists. To reveal the underlying driving mechanism of the influence of locomotive group size on train longitudinal surge behaviour, this section specifically establishes two comparative scenarios – namely, 'constant per-locomotive tractive effort' and 'constant total tractive effort' – to quantitatively evaluate the longitudinal dynamic evolution characteristics of multi-locomotive consists under frequent low-adhesion excitations.

5.3.1. *Constant per-locomotive tractive effort*

To investigate the influence of consist size on system surge characteristics when each locomotive approaches the adhesion limit, this section establishes three parallel simulation scenarios: '2 + 0' (four locomotives, two units), '3 + 0' (six locomotives, three units), and '4 + 0' (eight locomotives, four units) consists. In these cases, the tractive effort of each locomotive is kept the same, while the number of locomotives in the consist is varied. Therefore, the total tractive effort increases with the number of locomotives. It should be noted that the 2 + 0, 3 + 0, and 4 + 0 cases in this subsection were all initialised at the same train speed of 60 km/h. To eliminate the influence of different mean acceleration or deceleration caused by different total tractive efforts, the equivalent running resistance was set separately in each case so that the prescribed total tractive effort was balanced at the initial speed of 60 km/h. Therefore, the resistance-balance speed represented by all three cases is 60 km/h by construction. This setting is not intended to represent a normal speed-regulated service operation under the same physical track-resistance condition. Rather, it is a mechanistic sensitivity case designed to isolate the influence of locomotive number when each locomotive operates at a similar high adhesion-utilisation level. Since the

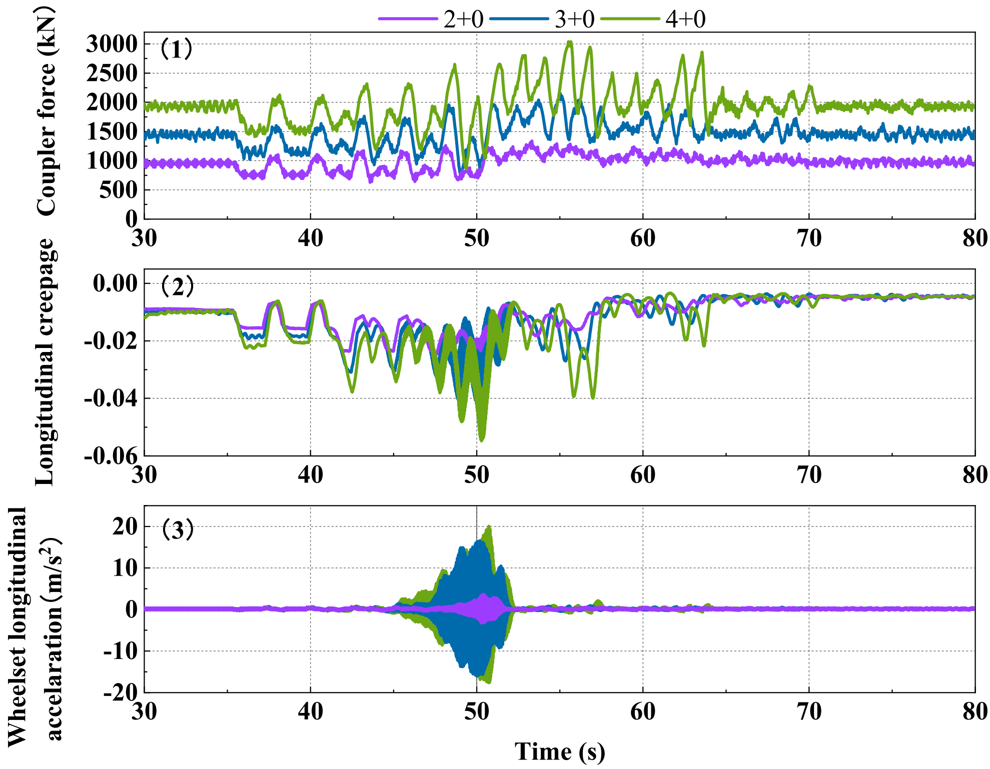

Figure 11. (1) Coupler force at the rear of the first wagon; (2) Wheelset longitudinal creepage; (3) Wheelset longitudinal vibration acceleration.

equivalent running resistance is not identical among the three cases, the results in this subsection should not be interpreted as a direct operational ranking of the 2 + 0, 3 + 0, and 4 + 0 consists. Instead, they are used to reveal the amplification mechanism of longitudinal surge when more locomotives participate in quasi-synchronous slip and re-adhesion under high adhesion utilisation. The operationally more comparable condition is discussed in Section 4.3.2, where the total tractive effort is kept constant and distributed among different numbers of locomotives.

Figure 11 presents the time-domain responses under different locomotive consist configurations, including the longitudinal coupler force at the rear of the first wagon, wheelset longitudinal creepage, and wheelset longitudinal vibration acceleration. A detailed analysis of the response curves yields the following observations: under the constant per-locomotive tractive effort condition, an increase in the number of locomotives within the consist tends to increase the amplitude of the longitudinal dynamic response.

Specifically, the differences in dynamic response among the three consist configurations. First, the response amplitude increases as the number of locomotives increases: as shown by the variations in wheelset longitudinal creepage in Figure 11(2) and wheelset longitudinal vibration acceleration in Figure 11(3)., the '2 + 0' consist (purple line) keeps all corresponding responses within the range of small fluctuations even under the prescribed adhesion-recovery transitions. In contrast, for the '4 + 0' consist (green line), the creepage

Table 2. Comparison results under different consist configurations.

Consist configuration	Maximum coupler force (kN)	Maximum coupler force oscillation amplitude (kN)	Maximum wheelset longitudinal vibration acceleration (m/s^2)
4 + 0	3040.2	1793.7	19.9
3 + 0	2152.6	1207.8	16.4
2 + 0	1338.5	591.1	3.5
Difference	41.2%/0/−37.8%	48.5%/0/−51.1%	21.3%/0/−78.7%

shows a marked variation during the 45–50 s interval, and the wheelset longitudinal vibration acceleration increases to approximately ± 20 m/s^2, indicating that the wheelset drive system develops a high-frequency stick–slip vibration response.. Second, the transient longitudinal coupler-force response is amplified. For the '3 + 0' (blue line) and '4 + 0' consists, the coupler force amplitude increases significantly, with peak values reaching approximately 2100 and 3000 kN, respectively. Third, the duration of the large-amplitude response becomes longer as the number of locomotives increases. After the rail adhesion conditions fully recovered at 50.5 s, the dynamic fluctuations of the coupler force in the '2 + 0' consist stabilised within about 8 s, whereas those in the '4 + 0' consist stabilised within about 20 s, representing a 150% increase in stabilisation time.

The aforementioned response amplification trend can be further explained through the longitudinal system dynamics mechanism of heavy-haul trains. According to fundamental dynamics theory, when a group of locomotives experiences synchronous or quasi-synchronous slipping and re-adhesion under low-adhesion excitation, the entire locomotive consist can be regarded as a concentrated source of transient excitation at the train head. The greater the number of locomotives, the larger the total effective mass ($\sum m_i$) participating in the synchronous excitation grows linearly. Consequently, under similar adhesion excitation and acceleration variation, the transient excitation transmitted from the locomotive group to the front of the train becomes larger This larger transient excitation is transmitted through the coupler and draft gear system to the adjacent freight-wagon connection. Therefore, increasing the number of locomotives under the constant per-locomotive tractive effort condition intensifies the coupling between locomotive-end stick–slip excitation and the longitudinal coupler-force response near the train head.

Quantitative data (Table 2) provide a clear illustration: taking the conventional '3 + 0' consist as a baseline, for the '4 + 0' consist, the absolute peak coupler force increases by 41.2%, the maximum differential of a single oscillation increases by 48.5%, and the high-frequency wheelset vibration acceleration deteriorates by 21.3%. In contrast, for the streamlined '2 + 0' consist, the corresponding impact indices plummet by 37.8%, 51.1%, and 78.7%, respectively.

5.3.2. Constant total tractive effort

To investigate the influence of power distribution on longitudinal surge characteristics under the same total tractive effort demand, this section compares two locomotive configurations with the same total tractive effort of 1500 kN: the '3 + 0' consist and the '4 + 0' consist. The wheel–rail friction coefficient and train speed settings are consistent with those in Section 4.1.

It should be noted that this section only selects the 3 + 0 and 4 + 0 consists for comparison under the constant total tractive effort condition. The reason is that, for the 10,000-tonne heavy-haul train and the long steep upgrade and low-adhesion conditions studied in this paper, the available traction capacity of the 2 + 0 consist is insufficient to reasonably provide the same total tractive effort. If the same total tractive effort were imposed on the '2 + 0' consist, each locomotive would operate under excessively high adhesion utilisation, and the comparison results would be affected by traction-capacity limitations effects. Therefore, this section focuses on comparing the 3 + 0 and 4 + 0 consists, both of which are capable of meeting the traction demand, in order to analyze how increased power distribution affects longitudinal dynamic response under the condition of constant total tractive effort.

Based on the time-domain dynamic response curves shown in Figure 12, the two consist configurations exhibit different response characteristics under the same total tractive effort condition. The '3 + 0' consist (blue curve) shows relatively large fluctuations in longitudinal coupler force and wheelset creepage under the prescribed adhesion-recovery excitation, indicating a stronger tendency toward longitudinal surge. In contrast, the '4 + 0' consist (green curve), when subjected to the same adhesion condition, shows smaller response amplitudes and a more stable longitudinal coupler-force response.

This difference can be explained by the reduced per-locomotive tractive effort in the '4 + 0' consist: Due to the more distributed traction power, the average tractive effort per locomotive in the '4 + 0' consist is reduced to 375 kN. As shown in Figure 12(4), this lower per-locomotive tractive effort keeps the wheel–rail operating points closer to the small-creepage region of the adhesion characteristic curve. In this region, the wheel–rail creepage remains far below the critical saturation peak, and the system exhibits positive creep damping (i.e. self-recovery capability). Consequently, even when subjected to **t**he same prescribed friction-coefficient variations, the wheel–rail creepage disturbance is more easily attenuated, and the longitudinal coupler-force fluctuation is reduced.

Based on the simulation results above, under the macroscopic condition of constant total tractive effort, increasing the number of locomotives in the consist **c**an reduce the per-locomotive adhesion utilisation. This helps move the wheel–rail operating point away from the high-creepage region associated with adhesion instability and improves the longitudinal dynamic response of the train.

5.4. Effect of locomotive adhesion control system

During the process of a heavy-haul train passing through a low-adhesion section and inducing longitudinal surge, the locomotive adhesion control system is often triggered at high frequency, resulting in multiple nonlinear 'unloading–recovery' cycles of traction force. To investigate the influence of the adhesion control system on the macroscopic longitudinal dynamic behaviour of the train, this section conducts a comparative simulation analysis under two operating conditions – without stick-slip control and with stick-slip control – using a '3 + 0' consist train with a total traction load of 1500 kN.

Figure 13 presents the time-domain evolution characteristics of the coupler force at the rear of the first wagon adjacent to the locomotive for the '3 + 0' consist train under conditions with and without intervention of the adhesion control system, supplemented by the

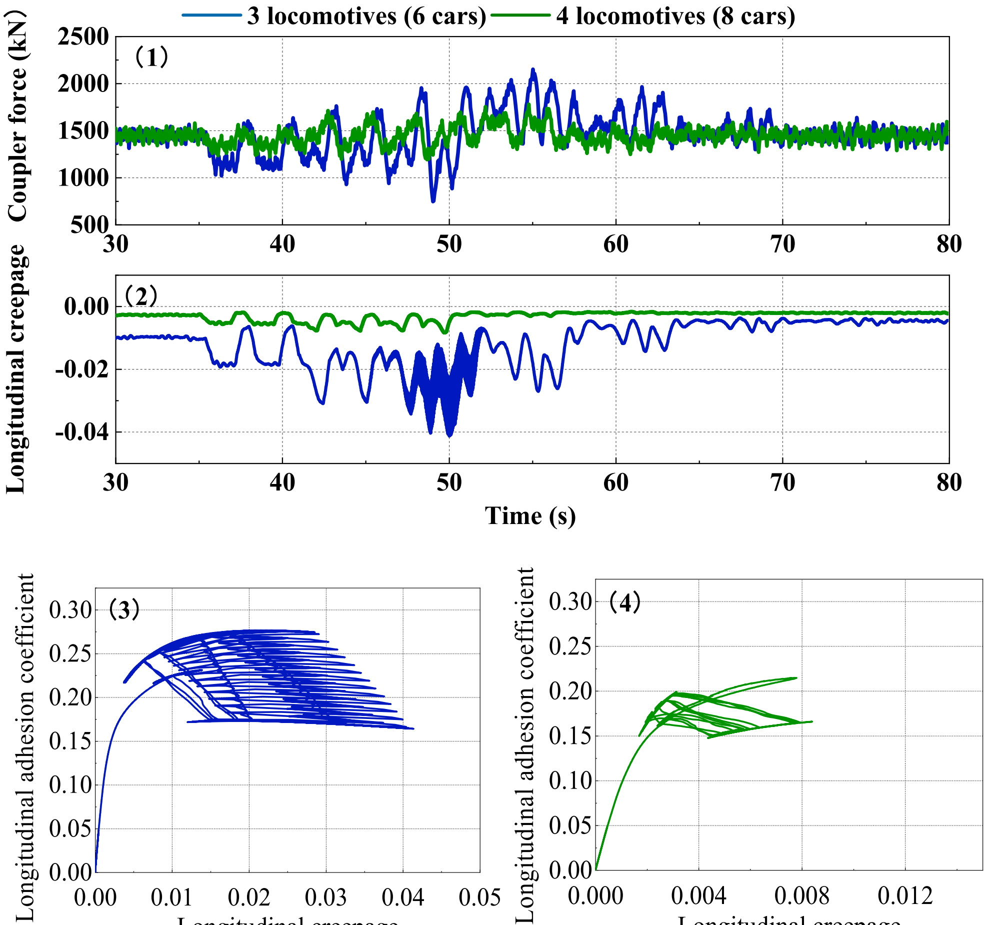

Figure 12. (1) Coupler force at the rear of the first wagon; (2) Wheelset longitudinal creepage; (3) Wheel–rail adhesion characteristic curve for the locomotive in the 3 + 0 consist; (4) Wheel–rail adhesion characteristic curve for the locomotive in the 4 + 0 consist.

response curves of the locomotive wheelset longitudinal creepage, and wheelset longitudinal vibration acceleration. The wheel–rail friction coefficient setting is consistent with that in Section 4.1.

From the evolution trend of wheelset longitudinal vibration acceleration, it can be observed that under the uncontrolled condition (blue curve), the wheelset exhibits a large-amplitude stick–slip vibration response around 48 s. The intervention of the adhesion control system (red curve) effectively suppresses this high-frequency oscillation, allowing the wheelset acceleration to rapidly decrease to a low-amplitude level. Owing to this local vibration suppression at the drive end, the positive peak of the longitudinal coupler force at the measured first-wagon location is effectively constrained, with its maximum value decreasing from 2152.7 kN under the uncontrolled condition to 1755.6 kN, representing a reduction of 18.4%. This indicates the effectiveness of adhesion control in reducing the peak transient longitudinal coupler force near the locomotive end.

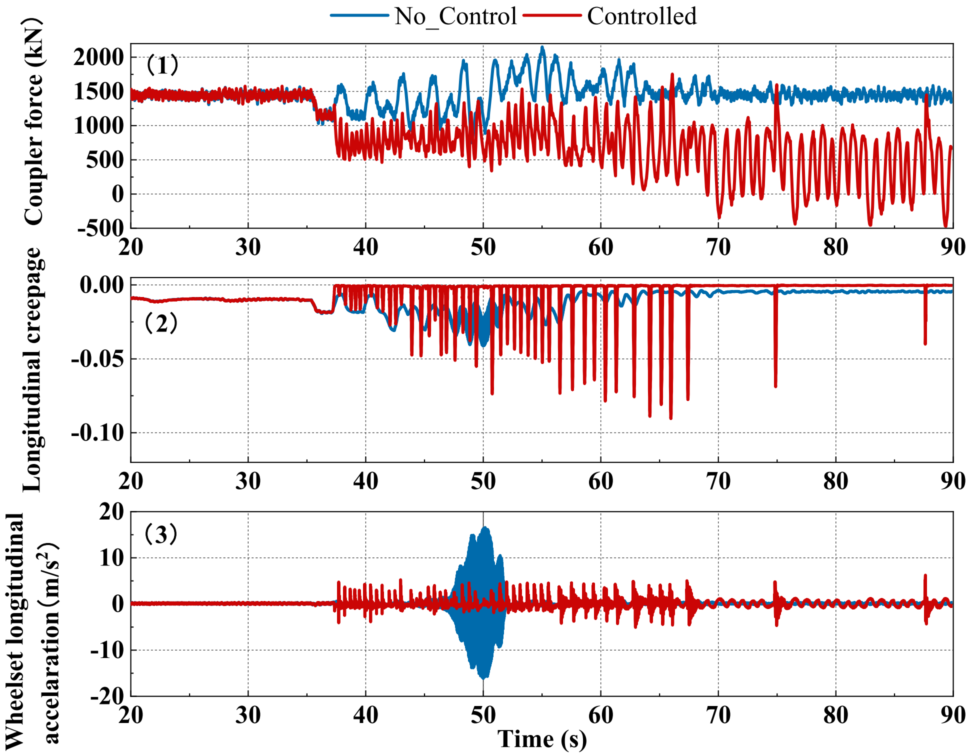

Figure 13. (1) Coupler force at the rear of the first wagon; (2) Wheelset longitudinal creepage; (3) Wheelset longitudinal vibration acceleration.

However, although the local high-frequency stick–slip vibration of the wheelset is suppressed, the time-domain response at the first-wagon coupler indicates an increase in low-frequency longitudinal coupler-force fluctuations near the locomotive end. A comparison of the coupler force curves reveals that the frequent intervention of the adhesion control system introduces repeated traction-force reduction and recovery processes, which are associated with sustained large-amplitude fluctuations in the measured coupler force, triggering large compressive components in the longitudinal coupler force at this measured location after 70 s. Quantitative data show that the peak-to-peak value of the dynamic coupler force fluctuations increases from 1405.5 kN to 2226.6 kN, an increase of 58.4%. Meanwhile, the longitudinal creepage exhibits repeated pulsed variations, indicating a stronger coupling between wheel–rail creepage dynamics and the front-end longitudinal coupler-force response.

Further analysis suggests that the conventional adhesion control system acts as a low-frequency external excitation source during the surge development phase. When transient axle load transfers or creepage fluctuations near the locomotive end induced by longitudinal surge trigger the anti-slip threshold, the system initiates a rapid reduction in traction force; after the slipping tendency subsides, torque is reapplied according to a preset ramp rate. This repeated abrupt variation in traction force enhances the low-frequency fluctuation of the longitudinal coupler force at the first-wagon location. More critically, severe coupler force fluctuations interfere with the system's ability to accurately identify the actual wheel–rail adhesion state, leading to misalignment in traction force regulation. These two effects interact and form a positive feedback mechanism, making it difficult for the train to restore stable operation and posing a significant threat to operational safety. It can thus be concluded that although the adhesion control system limits peak loads to a certain extent, the dynamic fluctuations it induces may contribute to sustained large-amplitude longitudinal coupler-force fluctuations near the locomotive end.

6. Conclusions

Based on a multi-scale co-simulation framework integrating train longitudinal dynamics, locomotive multi-body dynamics, and real-time control algorithms, this paper investigates the longitudinal surge phenomenon of 10,000-tonne heavy-haul trains under low-adhesion conditions. The main conclusions are as follows:

(1) The formation of surge in 10,000-ton trains is closely related to the nonlinear interaction between locomotive wheel–rail adhesion variation, drive-system stick–slip vibration response, and train longitudinal dynamics. During continuous sanding operations, the stepwise recovery of wheel–rail adhesion induces repeated traction-force fluctuations and local energy exchange in the wheelset–drive system; when the local stick–slip response becomes sufficiently strong, high-frequency vibration occurs at the wheelset–drive system level. This high-frequency excitation is transmitted through the coupler and draft gear system into the following wagon consist and further excite low-frequency longitudinal coupler-force fluctuations.

(2) The influence of the number of locomotives on longitudinal dynamic response exhibits significant differences depending on boundary conditions. Under constant per-locomotive tractive effort and high adhesion-utilisation conditions, increasing the number of locomotives in the consist increases the total excitation input at the train head and amplifies the longitudinal coupler-force response. In the simulated case, the maximum coupler force for the '4 + 0' consist increases by 41.2% compared with the '3 + 0' consist. Conversely, under constant total tractive effort, increasing the degree of power distribution reduces the adhesion utilisation of each locomotive and shifts the wheel–rail operating point farther from the high-creepage region associated with adhesion instability, thereby improving the longitudinal dynamic response of the train.

(3) Although conventional adhesion control systems can effectively suppress local high-frequency stick-slip instability of the wheelset and reduce the peak coupler force by 18.4% to mitigate transient overloads, their periodic 'unloading–recovery' torque regulation introduce repeated low-frequency traction disturbances into the longitudinal train system. This alternating disturbance causes a sharp 58.4% increase in the peak-to-peak value of coupler force fluctuations, indicating that frequent adhesion-control intervention contributes to sustained large-amplitude coupler-force oscillations near the locomotive end.

Author contributions

CRediT: **Qun Ma:** Conceptualization, Data curation, Formal analysis, Investigation, Writing – original draft, Writing – review & editing; **Wei Wei:** Conceptualization, Methodology, Resources, Writing – original draft; **Yuan Yao:** Conceptualization, Funding acquisition, Validation, Writing – review & editing; **Jiawen Sun:** Investigation, Software, Writing – original draft

Disclosure statement

No potential conflict of interest was reported by the author(s).

Funding

This work was supported by the National Natural Science Foundation of China (Grant Nos. 52372403 and U2268211), the National Railway Group Science and Technology Program (grant number N2025J026), the CRRC Original Technology Ten-Year Cultivation Special Project (2025CYY002), the Independent Project of the State Key Laboratory of Rail Transit Vehicle System (2026RVL-T04), and the Doctoral Innovation Fund Program of Southwest University (CX-2026ZD09).

ORCID

Yuan Yao http://orcid.org/0000-0003-2279-7463

References

[1] Wang J, Wang D. Discussion and application of safety strategies for 10,000-ton train operation. Sci Technol Innov Appl. 2017;1:276–277. doi:10.19981/j.cn23-1581/g3.2017.01.240
[2] Dong SJ. Simulation analysis of slope starting for heavy-haul combined trains [Master's thesis]. Da lian: Dalian Jiaotong University. 2025. doi:10.26990/d.cnki.gsltc.2025.000799. (in Chinese).
[3] Zheng YP, Wang JZ. Research and application based on technology of special difficult sections of heavy-haul railway. Shenhua Sci Technol. 2019;17(08):77–81. (in Chinese).
[4] Wang J, Wang D, Wang B. Analysis and research on longitudinal impulses in ultra-long heavy-haul trains on long steep upgrades. Energy Sci Technol. 2025;23(03):81–84. (in Chinese).
[5] Yang L, Luo S, Fu M, et al. Effects of mixed marshalling modes on longitudinal freight train dynamics. Proceedings of the Institution of Mechanical Engineers, Part F: Journal of Rail and Rapid Transit. 2023;237(8):1060–1071. doi:10.1177/09544097231151477
[6] Liang J. Research on longitudinal and lateral loads of heavy-haul trains [dissertation]. Chengdu: Southwest Jiaotong University; 2013; (in Chinese).
[7] Zhai WM, Stichel S, Ling L. Train-track coupled dynamics problems in heavy-haul rail transportation. Veh Syst Dyn. 2025;63(7):1187–1240. doi:10.1080/00423114.2025.2494834
[8] Cole C, Sun YQ. Simulated comparisons of wagon coupler systems in heavy haul trains. Proceedings of the Institution of Mechanical Engineers, Part F: Journal of Rail and Rapid Transit. 2006;220(3):247–256. doi:10.1243/09544097JRRT35
[9] Cole C. Longitudinal train dynamics. In: Iwnicki S, editor. Handbook of railway vehicle dynamics. Boca Raton: CRC Press; 2006. p. 239–278.
[10] Garg VK, Dukkipati RV. Dynamics of railway vehicle systems. Toronto: Academic Press; 1984.
[11] Iwnicki S, Handbook of railway vehicle dynamics. 2nd ed. Boca Raton: CRC Press; 2020.
[12] Wu Q, Cole C, Spiryagin M, et al. A review of dynamics modelling of friction draft gear. Veh Syst Dyn. 2014;52(6):733–758.
[13] Wu Q, Yang X, Cole C, et al. Modelling polymer draft gears. Veh Syst Dyn. 2016;54(9): 1208–1225. doi:10.1080/00423114.2014.894199

[14] Sun YQ, Cole C, Spiryagin M, et al. Dynamic characteristics of a new polymer draft gear for heavy haul trains. Proceedings of the Institution of Mechanical Engineers, Part F: Journal of Rail and Rapid Transit. 2017;231(5):567–578. doi:10.1080/00423114.2016.1196822
[15] Wang W, Guo L, Wang K, et al. Experimental and numerical study of the dynamic behavior of a heavy haul coupler with arc surface contact. Veh Syst Dyn. 2020;58(9):1345–1365.
[16] Wei W, Hu Y, Wu Q, et al. An air brake model for longitudinal train dynamics studies. Veh Syst Dyn. 2017;55(4):517–533.
[17] Wu Q, Spiryagin M, Cole C, et al. International benchmarking of longitudinal train dynamics simulators: results. Veh Syst Dyn. 2018;56(3):343–365. doi:10.1080/00423114.2016.1254261
[18] Wu Q, Cole C, Spiryagin M, et al. Freight train air brake models. Int J Rail Transp. 2023;11(1):1–49. doi:10.1080/00423114.2017.1377840
[19] Oprea RA, Cruceanu C, Spiroiu MA. Alternative friction models for braking train dynamics. Veh Syst Dyn. 2013;51(3):460–480. doi:10.1080/23248378.2021.2006808
[20] Bosso N, Magelli M, Zampieri N. A numerical method for the simulation of freight train emergency braking operations based on the uic braked weight percentage. Railw Eng Sci. 2023;31(2):162–171. doi:10.1080/00423114.2012.744459
[21] Pfaff R. Braking distance prediction for vehicle consist in low-speed on-sight operation: a monte carlo approach. Railw Eng Sci. 2023;31(2):135–144. doi:10.1007/s40534-022-00296-9
[22] Wei W, Zhang Y, Zhang J, et al. Influence of quick release valve on braking performance and coupler force of heavy haul train. Railw Eng Sci. 2023;31(2):153–161. doi:10.1007/s40534-023-00303-7
[23] Ge X, Chen Q, Ling L, et al. An approach for simulating the air brake system of long freight trains based on fluid dynamics. Railw Eng Sci. 2023;31(2):122–134. doi:10.1007/s40534-022-00301-1
[24] Pugi L, Rindi A, Ercole AG, et al. Preliminary studies concerning the application of different braking arrangements on Italian freight trains. Veh Syst Dyn. 2011;49(8):1339–1365. doi:10.1007/s40534-022-00291-0
[25] Di Gialleonardo E, Cazzulani G, Melzi S, et al. The effect of train composition on the running safety of low-ffatcar wagons in braking and curving manoeuvres. Proc Inst Mech Eng Part F J Rail Rapid Transit. 2017;231(6):666–677. doi:10.1080/00423114.2010.505291
[26] Cantone L. Traindy: the new union international des chemins de fer software for freight train interoperability. Proc Inst Mech Eng Part F J Rail Rapid Transit. 2011;225(1):57–70. doi:10.1177/0954409716636923
[27] Belforte P, Cheli F, Diana G, et al. Numerical and experimental approach for the evaluation of severe longitudinal dynamics of heavy freight trains. Veh Syst Dyn. 2008;46(S1):937–955. doi:10.1243/09544097JRRT347
[28] Wei W, Lin Y. Simulation of a freight train brake system with 120 valves. Proceedings of the Institution of Mechanical Engineers, Part F: Journal of Rail and Rapid Transit. 2009;223(1):85–92. doi:10.1080/00423110802037180
[29] Kalker JJ. Three-dimensional elastic bodies in rolling contact. Dordrecht: Kluwer Academic Publishers; 1990.
[30] Polach O. Creep forces in simulations of traction vehicles running on adhesion limit. Wear. 2005;258(7-8):992–1000.
[31] Zhang WH, Chen JZ, Wu XJ, et al. Wheel/rail adhesion and its influence on locomotive traction. Veh Syst Dyn. 2002;37(sup1):123–135. doi:10.1016/j.wear.2004.03.046
[32] Arias-Cuevas O, Li Z, Lewis R. A laboratory investigation on the influence of the particle size and slip during sanding on the adhesion and wear in the wheel-rail contact. Wear. 2011;271(1-2):14–24.
[33] Yao Y, Zhang HJ, Li YM, et al. The dynamics study of locomotive under saturated adhesion. Veh Syst Dyn. 2011;49(8):1321–1338. doi:10.1016/j.wear.2010.10.050
[34] Yao Y, Zhao SY, Xiao FX, et al. The effects of suspension parameters of wheelset driving system on the re-adhesion performance of locomotives. Veh Syst Dyn. 2015;53(12):1935–1951. doi:10.1080/00423111003668195

[35] Spiryagin M, Wolfs P, Szanto F, et al. Co-simulation of a mechatronic system for locomotives with adhesion control. Veh Syst Dyn. 2015;53(5):673–689. doi:10.1080/00423114.2015.1108446
[36] Allotta B, Pugi L, Ridolfi A, et al. An innovative adhesion estimation algorithm for railway vehicles. IEEE Trans Veh Technol. 2014;63(8):3572–3582.
[37] Pichlik P, Zdenek J. Overview of slip control methods used in locomotives. Transactions on Electrical Engineering. 2019;8(2):38–45.
[38] Wang J, Wang D, Wang B. Analysis and research on longitudinal impulses in ultra-long heavy-haul trains on long steep upgrades. Energy Sci Technol. 2025;23(03):81–84. (in Chinese).
[39] Zhang QM, Zhong PH, Zhu L. Research on finite set predictive control for surge of 10,000-ton heavy haul trains on Shenmu-Shuozhou railway. Electric Drive for Locomotives. 2024;1:93–100. (in Chinese).
[40] Guo XR, Ling L, Zhai WM. Traction control strategy for suppressing surge of heavy-haul trains on long steep upgrades. In: Proceedings of the 16th National Conference on Vibration Theory and Applications: Chengdu. 2025:19–24. doi:10.26914/c.cnkihy.2025.125696
[41] National Railway Administration of the People's Republic of China. Railway train traction calculation part 1: trains with locomotives (TB/T 1407.1-2018). Beijing: China Railway Publishing House; 2018; (in Chinese).
[42] Yang HU. Longitudinal dynamic test and simulation study on Shen-hua 10000t heavy haul train. Dalian: Dalian Jiaotong University; 2017; (in Chinese).
[43] Zhao XB. Research on optimization of draft gear characteristics of railway freight cars. Dalian: Dalian Jiaotong University; 2017; (in Chinese).
[44] Zhu JC, Liu FY, Dong SJ, et al. Gradient starting method and longitudinal dynamics characteristics of heavy-haul trains. Engineering Mechanics.2026; https://link.cnki.net/urlid/11.2595.O3.20250220.1553.004.
[45] Yao Y, Zhang XX, Zhang HJ, et al. The stability mechanism and its application to heavy-haul couplers with arc surface contact. Veh Syst Dyn. 2013;51(9):1324–1341.
[46] Shi Z, Wang K, Guo L, et al. Effect of arc surfaces friction coefficient on coupler stability in heavy haul locomotives: simulation and experiment. Veh Syst Dyn. 2017;55(9):1368–1383. doi:10.1080/00423114.2013.801500